Evolution of galaxy dynamics over the last 10 Gyrs with MUSE/VLT

Master Thesis

Author: Mercier Wilfried
Supervisor: Contini Thierry
Co-Supervisor: Epinat Benoît

Observatoire de Paris

Institut de Recherche en Astronomie et Planétologie

Laboratoire d'Astrophysique de Marseille

June 4, 2019

Abstract

Contents

List of Figures

List of Tables

1   Introduction

1.1   Current topics in galactic astronomy

1.1.1   A global picture of the Universe

Our knowledge of galaxy properties and their evolution through time has drastically changed from the early 20th century when the Grand Debate (Shapley & Curtis, 1921) between Harlow Shapley and Heber Curtis on the (extra)galactic origin of the so-called nebulae took place (see Trimble (1995) for an interesting discussion on the subject). Since Hubble (1926), Hubble (1929) measurement of these nebulae distance to us, we now they actually are galaxies like our own lying at great distances and moving away from us. This global movement was understood in the cosmological framework of an expanding Universe. In a few months of interval, in 1998-1999, two teams measured the redshift and distance of far distant type Ia supernovae, considered as standard candles, and held evidence for an accelerating expansion which revived the need of a cosmological constant in Einstein's field equations (Riess et al., 1998), (Perlmutter et al., 1999). This additional term has been interpreted as a fluid with negative pressure acting against gravity, and is known as dark energy. Additionally, the first evidence of a dark component in galaxy clusters mass distribution was suggested by Fritz Zwicky (Zwicky, 1933), (Zwicky, 1937). By measuring the relative velocity of 7 galaxies in Coma Berenices, he derived a velocity dispersion σ_{v} from which he computed with the virial theorem an order of magnitude for the dynamical mass $M_{\mathrm{d}} \sim (\sigma_{\mathrm{v}}^2 R)/G$ with R the cluster characteristic size. The given mass was roughly two orders of magnitude above the expected luminous mass from the luminosity of the galaxies. However, this argument never really convinced the other astronomers at the time. A stronger proof for the existence of a dark component embedded in galaxies came from the study of galaxy rotation curves performed by Vera Rubin in the 1970s (Rubin & Ford, 1970), (Rubin et al., 1978). By looking at the outer material of galaxies, she observed flat rotation curves which either indicated a deviation from Newton's law of gravitation or the presence of large amounts of dark matter in surrounding haloes.

From this point onward, the need of a unified cosmological model including these new aspects became obvious. Though other models trying to describe dark mater as a manifestation of a modified newtonian gravity (here insert citation to some MOND paper) exist, decades of observations, state of the art N-body simulations and measurements of cosmological probes have given the actual ΛCDM model its renown. In the meantime, as cosmology advanced and the size of the Universe exploded following Hubble 1929 publication, a new branch of astronomy centred on galaxies quickly developed both in terms of observations and of theoretical modelling.

1.2   What we have learned about galaxies so far

1.2.1   Evolving properties with redshift ?

Nowadays, galaxies are understood as gravitationally bound collections of stars, gas and dust which are supposed to have collapsed from initial clouds embedded in rapidly growing dark mater haloes. Galaxies formation and evolution should therefore follow the growth of the dark matter distribution through space and time, and as such should be tightly correlated to the global properties of our Universe.

In the local Universe, galaxies can be divided into two categories based on their shape and colour: red ellipticals and blue spirals. These are also referred to as early and late type respectively according to Hubble (1922), Hubble (1926) classification. Even though this is true for most galaxies, we also observe a small fraction of dustier red spirals. Nevertheless, the separation is clear with very few galaxies in between the two populations. Ellipticals tend to be the most massive ($M \sim 1 - 5 \times 10^{11} \mathrm{M_\odot}$), as well as quenched, that is their Star Formation Rate (SFR) is near 0. Most of their massive younger and bluer stars are gone (as a star's lifetime scales as its mass to the power of 3 or so) leaving only old red stards, which is the reason for their red colour. On the other hand, spirals are more recent, star-forming galaxies, still full of blue stars, but also smaller and lighter. When looking at more distant parts of the Universe, say $z > 0.5$, this dichotomy is less pronounced. Giant ellipticals are more rare, those found are still forming stars and disk-like galaxies have more irregular morphologies which might be due to past merger events or unrelaxed kinematics because of a recent formation.

Assigning a characteristic velocity and a velocity dispersion, which are two key parameters used virtually in every kinematical study, to a galaxy is not a straightforward step. Generally, this is done by fitting a model onto some velocity measurement which requires spectroscopic data (2D image or slit). Following Vera Rubin pioneering work, almost all galaxies are found to have flat rotation curves because of their dark matter content (except perhaps for some dwarf galaxies but these are too small to be detected at high redshift). By flat, we mean that they have a steadily rising slope from the central part until it reaches a turnover point where the curve flattens, a so-called plateau, or where it slowly decreases. In this case, the characteristic velocity which is taken into account is, most of the time, the maximum velocity at the turnover, or the plateau velocity V_{max}. On the other hand, there are various ways of computing the velocity dispersion σ_{v}, but all ultimately describe the amplitude of unordered, incoherent motion within the galaxy.

In the local Universe, most spirals have low velocity dispersion compared to their rotational velocity. The opposite is true for elliptical galaxies with high velocity dispersion but no significant rotation. For more distant galaxies, this might not be true any

more with a much higher fraction of spiral or disk-like galaxies[1] with high velocity disper-
sion. Usually, the parameter $V_{\max}/\sigma_v$ is used to classify a galaxy as either rotationnaly
supported (> 1) or as dispersion dominated (< 1). High redshift dispersion dominated
galaxies were first discovered by (insert Erb et al 2006a paper here). These are different
from the "dispersion dominated" giant ellipticals we see in the local Universe as they are
less massive, more compact and yet highly star forming. Some authors hypothesized that
the dispersion dominated galaxies are ancestors of the modern large ellipticals, growing
by subsequent merging, or perhaps just the ancestors of the few small ellipticals we see
today. Nevertheless, if there is any relation between these two populations, it is still not
clear what it is. As we do not know if these dispersion dominated systems are due to
unresolved rotation, investigation of the kinematics of new data with better spectral and
spatial sampling is mandatory.

1.2.2   An impact from the environment ?

Theoretical modelling based on simple physics principles such as angular momentum con-
servation, viscous friction, dissipation of energy or gravitational instabilities can account
for both the global morphology and kinematics of galaxies. Though state of the art N-
body simulations including other components such as stellar feedback from supernovae,
Active Galactic Nuclei (AGN) in the centre of galaxies with their outflows and inflows
from filaments of gas in the large scale structure of the Universe, have shown that these
new mechanisms have more impact on the kinematics than previously thought. Never-
theless, seeing more disturbed morphologies and systems with high velocity dispersion at
high redshift seems consistent with the hierarchical growth of dark matter haloes which
drive the evolution of galaxies. In this regard, and as haloes will bound galaxies and
gas together, we might expect to find a larger fraction of unrelaxed interacting and/or
merging galaxies in these parts than for field galaxies, that is those which do not belong
to any structure.

The galaxies star formation is also strongly dependent on both the morphology and the
redshift. It can be computed either from a gas density measurement, using a scaling law
between with the Star Formation Rate (SFR) density, or by computing a Star Formation
History (SFH) from Spectral Energy Distribution (SED) fitting techniques if a spectrum
of the galaxy is available. Observations and measurements of galaxies SFRs through large
redshift intervals have shown that it changed through time, increasing first till a redshift
of about $2 - 1.5$ and then starting to decrease. Nowadays, we are in this phase, and
indeed, we observe less blue star forming galaxies and more red quenched ellipticals in
our surroundings than in more distant parts of the Universe. Quenched galaxies

---

[1]We will preferentially use the terms disk-like/late-type galaxies rather than spiral as some galaxies
studied in the present work do show a disk morphology without clear spiral arm patterns.

1.3 Photometry and spectroscopy

1.3.1 Differences between spectroscopy and photometry

Studying questions related to the formation and evolution of galaxies requires large datasets of objects at low and high redshifts. The two type of observation which can be carried out to answer these questions are photometry and spectroscopy. These methods were originally independent, yielding unique information on the different components of the galaxies, their distribution, the morphology and the kinematics of these galaxies. Photometry yields 2D images of galaxies whose surface brightness, that is its total flux divided by its solid angle on the sky, is above the surface brightness limit imposed by the instrument limitations, but also whose size is above the instrument resolution. Depending on the band used, we can observe different galactic components, ranging from the cold, hot and ionised gas to young/old stellar populations, as well as dust. On the other side, spectroscopy give us information on the strength of the components in the total emitted light by looking at continuum and emission lines. Galaxy spectra can contain high continuum values coming from the combination of old and young stellar populations spread through the galaxy. Detected emission lines, such as Hα, Hβ, [OII] and [OIII] doublets or Lyα give us insight into the presence of gas and its ionisation, which can in turn indicate the presence of star-forming regions within the galaxy such as [HII] regions. On the contrary, absorption lines tell us about the existence of gas on the line of sight which can be either outside of the galaxy, or directly inside (self-extinction).

Having 2D images from photometry, it seems natural to derive morphological parameters, such as the ellipticity $e = 1 - b/a$ with b and a the minor and major axes respectively, or a measure of some characteristic radius. Generally, it is assumed that the galaxies light profile has high degrees of symmetry. This implies that a galaxy with an inclination[2] $i = 0°$ should have circular isophotes (lines of identical surface brightness). When elliptical isophotes are seen, which implies an elliptical shape for the galaxy, this is an indication of a non-zero inclination. Based on our definition, this translates in terms of ellipticity as

$$\cos i = 1 - e \tag{1}$$

This assumption is invalid in reality as galaxies have more complex morphologies with central bars, spiral arms, satellite galaxies for the largest ones and potential inflows and/or outflows. It is also incorrect when studying galaxies which have clear disturbed morphologies due to past interactions such as merging events.

---

[2]We define the inclination as the angle between the plane of the galaxy and the plane of the sky, or equivalently between the normal to the plane of the galaxy and the line of sight.

In the past, measuring radii and ellipticity were generally done by hand with a method using the curve of growth and which consisted in deriving the size and ellipticity of ellipses at different isophote levels. Nowadays, it has become common to fit galaxy light profile models onto images and to recover the morphological parameters from the best fit. One of the most commonly used light profile is a Sérsic profile which we generally write as (Graham et al., 2005)[3]

$$I(r) = I_{\mathrm{e}} e^{-b_n \left(\left(\frac{r}{R_{\mathrm{e}}} \right)^{1/n} - 1 \right)} \tag{2}$$

where r is the radial distance to the morphological centre of the galaxy, n is referred as the Sérsic index of the galaxy, R_e is the effective or half-light radius which encloses 50% of the total luminosity of the galaxy, I_e is the intensity at the position R_e and b_n is a term which ensures that R_e does enclose half the total luminosity. The formal definition of b_n can be shown to be such that $2\gamma(2n, b_n) = \Gamma(2n)$ with γ and Γ respectively the incomplete and complete gamma functions.

This equation has been widely used in different context because of its ability to recover two famous profiles:

- an exponential disc for $n = 1$ which represents a disk-like/spiral galaxy. In this case, r generally represents the radial distance in the galactic plane. Sometimes, two exponential discs are used to represents the vertical variation of the emitted light as well as in the plane of the galaxy.

- a de Vaucouleurs profile for $n = 4$ which describes elliptical (early-type) galaxies

Depending on the author, only a single Sérsic profile with a freely varying Sérsic index can be used, as is the case for softwares such as SExtractor (Bertin & Arnouts, 1996) or GIMD2D (Simard, 1998). Sometimes, others prefer to use a combination of a bulge and a disk components, with two fixed Sérsic indices. This is the case in GALFIT (Peng et al., 2002).

Studying galaxy spectra can also be quite a challenge. These can have a noisy continuum emission which can make difficult the detection of emission lines. In general, astronomers look at specific spectral features such as Balmer or Lyman lines, or doublets to improve the confidence in the detection. However, spectroscopes only work in a certain spectral domain, and therefore any line falling out the instrumental range cannot be detected. Given the usual relation between the observed and emitted wavelengths $\lambda_{\mathrm{obs}} = \lambda\mathrm{em}(1 + z)$ with z the redshift of the galaxy, observing some line in a limited

---

[3]The original definition $I(r) \propto e^{(r/\alpha)^{1/n}}$ from Sérsic (1963) was modified to Eq. 2 because of the too small (immeasurable) values α generally takes.

wavelength range implies that galaxies can only be detected in a certain redshift interval.

Detecting such lines is done through line fitting on a continuum subtracted spectrum. Many algorithms exist with slight variations but, generally, visible lines are fitted one after another with Gaussian shaped profiles. Since all of the emission lines of a given object are redshifted by the same amount, it is possible, based on the relative positions of the different detected lines, to know from which species it comes from and therefore to deduce the redshift of the object. In some cases, it is even possible to detect sources whose spectra are blended on the line of sight. Once the lines are detected, these can be studied individually to derive useful spectral parameters. For instance, measuring the total flux and determining how it compares to the continuum level allows one to derive a Signal to Noise Ratio (SNR), which can in turn be used when performing statistics on the data.

In theory, lines should be intrinsically infinitely thin, but in practice they have a certain width which is directly related to the properties of the emitting species and the physical processes at work in its environment. Assuming Local Thermodynamical Equilibrium (LTE) conditions are met, local variations of velocity due to temperature fluctuations will result in a Gaussian thermal Doppler profile. Turbulent motion will add another Gaussian term because of the variations of the mean velocity of the particles on the line of sight. On the other hand, natural and collision-driven widening of the rays both produce Lorentzian line profiles. In practice, all these processes occur at the same time but with different strength. This results in a ray which is made of a convolution of Gaussian and Lorentzian shaped profiles, which is known as a Voigt profile.

For some surveys of the sky such as the Sloan Digital Sky Survey (SDSS), photometric data is available in multiple bands. These surveys combine photometric and spectroscopic data, though the spectral resolution in this case is very low because of the few bands used and their wavelength range. For some objects, spectroscopic follow ups are performed, so that we have both precise photometric and spectroscopic data. However, these kind of surveys with follow ups, have two major flaws. First, it takes double time of observation for the same object as photometry and spectroscopy are performed with two different instruments. The other flaw is that there are only a handful of galaxies with spectroscopic follow ups since not all the objects can be observed. This induces to select objects based on astronomers' interests, which can in turn induces biases in the observed properties.

1.3.2   Spectroscopy

1.3.3   MUSE-VLT

MUSE is an Integral Field Unit (IFU) mounted on the VLT in Chile which spans a $1' \times 1'$ Field of View (FoV). Its wavelength range covers both the visual spectrum and the Near Infra-Red part (NIR), going from $4650\,\text{Å}$ to $9300\,\text{Å}$. This instrument was built with the main purpose of performing blind searches of sources in the field. The wavelength range is well suited to detect the OII doublet in the redshift range 0.4, 1.4.

2   Sample selection

2.1   MUSE-GTO MAGIC

2.2   COSMOS field

Group ID[1]	Ra[2] J2000 (°)	Dec[3] J2000 (°)	Exposure[4] (hr)	Average seeing[5] (")	Total nb. galaxies[6]	Nb. field galaxies[7]
CGr32	NaN	NaN	3×4.35	0.51 - 0.58	NaN	NaN
CGr34_d	149.87766	2.502331	5.25	0.63	NaN	NaN
CGr34_bs	149.87766	2.502331	4.75	NaN	NaN	NaN
CGr30_d	150.144225	2.065971	9.75	0.67	NaN	NaN
CGr30_bs	150.144225	2.065971	6.25	NaN	NaN	NaN
CGr84	150.057219	2.599744	5.25	0.59	NaN	NaN
CGr84-N	NaN	NaN	1	0.51	NaN	NaN
CGr114	149.994285	2.258044	2.2	0.68	NaN	NaN
CGr79	149.820686	1.821825	4.35	0.60	NaN	NaN
CGr28	150.218094	1.812667	1	0.62	NaN	NaN
CGr26	150.492767	2.069139	1	0.59	NaN	NaN
CGr61	149.728741	1.915987	1	0.64	NaN	NaN
CGr51	149.982756	1.801899	1	$0.6 - 0.7$	NaN	NaN
CGr23	149.790782	2.162648	1	0.68	NaN	NaN

Table 1: Main characteristics of the observed MUSE fields. Groups ending with _d correspond to deep observations (full stacked OBs) and with _bs correspond to best-seeing observations (only OBs with a seeing below 0.7"). The seeing is given for the [OII] wavelength at the group's redshift. 1. MUSE group number, 2. Group centre's right ascension, 3. Group centre's declination, 4. Duration of observations, 5. Average seeing during observation, 6. Total number of detected galaxies within MUSE FoV, 7. Number of field galaxies found by the FoF algorithm.

The point of the analysis is to perform a joint study of the morphology and the kinematics of field galaxies in the COSMOS area (Scoville et al., 2007) using respectively HST ACS images and MUSE data. To this end, a set of 12 galaxy structures (groups or clusters) was selected. The choice of the COSMOS area for this analysis was made because of the large number of multi-band photometric data available for the galaxies in this field and the presence of rich galaxy groups.

Guaranteed Time Observations (GTO) centred on the groups were performed from which 14 different MUSE Fields of View (FoV) of $1 \times 1\,\text{arcmin}^2$ were obtained. Each is composed of multiple Observation Blocks (OB) of $40 - 60\,\text{min}$ each with the Position Angle (PA) of the instrument rotated by 90° between consecutive exposures.

Most of the groups enter into one MUSE FoV, except for CGr32. Since this group is more extended than the others, three slightly overlapping FoVs were taken around

it. A couple of groups were also split into *deep* and *best-seeing* observations, the former combining all the OBs regardless of the average seeing in each OB, when the latter only kept OBs with an average seeing lower than 0.7".

The main characteristics of the observed FoVs, including the position of their centre, the exposure per FoV, the average seeing during the observation, the total number of galaxies and the number of field galaxies detected by the FoF algorithm are listed in Table 1.

These structures were chosen from (Knobel et al., 2009), (Knobel et al., 2012) catalogues. This ensured them to have both a large set of corresponding photometric data available from Laigle et al. (2016) catalogue and HST images with a much better resolution (0.03 arcsec/px for HST and ≈ 0.2 arcsec/px for MUSE). A few galaxies in CGr30_deep and around some stars might have also been detected within the data cubes but not in HST images. In the former case, the reason is that a blind source detection was performed with ORIGIN (Bacon et al., 2017) which can deblend sources even below the PSF. For the latter, this is because galaxies were detected in areas around stars which were masked when creating Laigle et al. (2016) catalogue.

2.3   Prior information on the galaxies

2.3.1   Galaxies in structures

This internship was planned to be similar in many aspects to what is doing V. Abril-Melgarejo, a 2nd year PhD student supervised by B. Epinat at LAM, Marseille. She studies the morphology and the kinematics of the galaxies within the structures observed with MUSE in the same fields as those we are using in this work. The main difference is that we are focusing on "field" galaxies when she only studies those in structures. To differentiate between group and field galaxies, a Friend of Friends algorithm (FoF) was run prior to my arrival on the galaxies in the MUSE fields. Thus, each galaxy was labelled either as belonging to a structure or as a "field" galaxies. Additionnaly, a morphological analysis had already been performed by V. Abril-Melgarejo with GALFIT on galaxies in structures only. Two Sérsic profiles with fixed Sérsic indices ($n = 1, 4$) were used to describe these galaxies as a combination of a disk and a bulge component. Hence, their intensity can be written as

$$I(r) = I_{e,\mathrm{d}}\, e^{-b_1\left[\frac{r}{R_\mathrm{d}} - 1\right]} + I_{e,\mathrm{b}} e^{-b_4\left[\left(\frac{r}{R_\mathrm{b}}\right)^{1/4} - 1\right]} \tag{3}$$

where $I_{e,\mathrm{d}}$, $I_{e,\mathrm{b}}$ are the effective intensities of the disk and the bulge component respectively and R_d, R_b their half-light radii.

Therefore, we already have in hand morphological information for roughly half of

the total sample including model parameters as described above, but also morphological parameters such as the ellipticity of the galaxies, the position angle of their kinematical main axis (which can be different from the morphological PA).

2.3.2   Morphological information from COSMOS catalogues

The total number of galaxies detected in the 14 MUSE fields in the COSMOS area is around 1000. Roughly half of them belong to structures and the other half are labelled as "field" galaxies. However, not all of them are useful to our study. Some may be too close to the edge for detection, others may be too noisy with a low SNR, or even too small, preventing any relevant kinematical modelling. It is thus mandatory to apply a selection on our data set of field galaxies, first to save time for the analysis, but also to reduce uncertainties.

Our goal is to perform a joint study of the morphology and the kinematics of these galaxies. The tools and the models for the kinematical modelling were already developed as they were used by V. Abril-Melgajero. On the other hand, fitting morphological models with software such as GalFit or SExtractor would have required additional time which we did not have. Hopefully for us, morphological modelling had already been performed on the galaxies in the COSMOS field, so we could focus on the kinematical part.

Morphological information for all the galaxies in COSMOS can be found in various catalogues and tables[4]. To start with, we decided to use the two most complete catalogues we could find, that of Tasca (maybe citation) and Cassata (maybe citation as well). Both catalogues contain morphological information including the central position of the galaxy, its half-light radius, concentration and asymmetry parameters, ellipticity, PA of the major morphological axis, and so forth for roughly 232000 galaxies. The authors obtained morphological information by running SExtractor on HST images of the galaxies in Laigle et al. (2016) catalogue.

Since we already had in hand a catalogue combining spectroscopic information (emission line fluxes, redshift, etc.) from MUSE measurements with photometric data from Laigle et al. (2016), we cross-matched it with Cassata's and Tasca's tables to collect their morphological parameters. We cross-matched first with each catalogue separately, and then with both, using the right ascension α and declination δ of the centre of the galaxies, allowing for a maximum separation between the MUSE source and the closest source within the catalogues of 1 arcsec maximum. This procedure was done for structure galaxies as well in order to use them to check the consistency of the catalogues parameters.
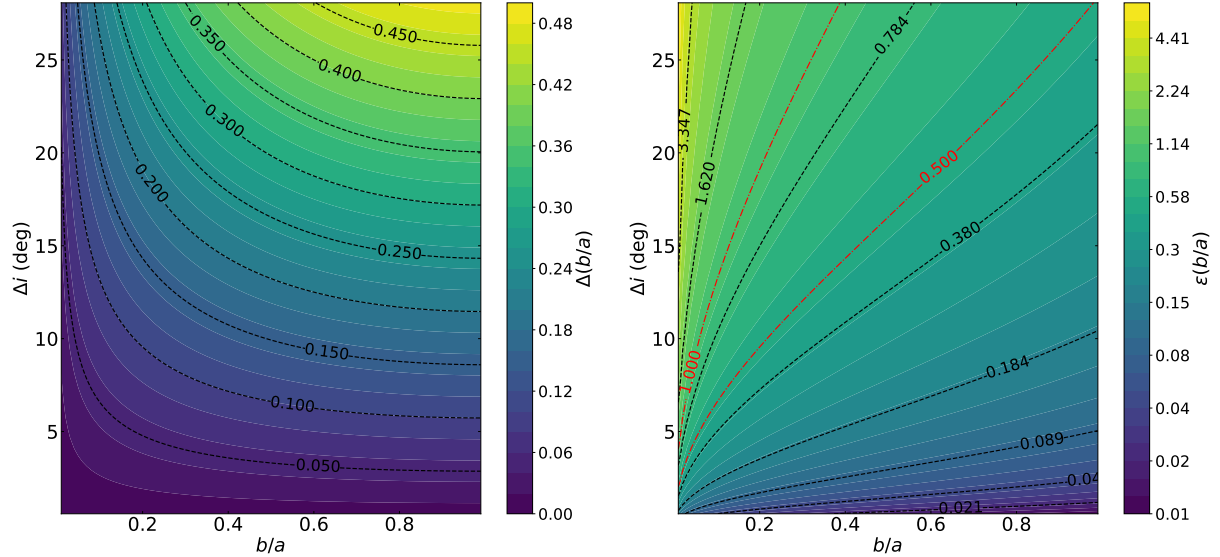
---

[4]`https://irsa.ipac.caltech.edu/data/COSMOS/tables/morphology/`

2.4   Checking catalogues values consistency

2.4.1   Reasons for checking catalogues values

(a) Error on inclination as a function of b/a and its absolute error. Contours of $\Delta(b/a)$ are plotted in black dashed lines with their corresponding value.

(b) Error on inclination as a function of b/a and its relative error. Contours of $\epsilon(b/a)$ are plotted in black and red dashed lines with their corresponding value.

Figure 1: Error on inclination as a function of b/a and its error. Left: as a function of the absolute error on b/a ($\Delta(b/a)$). Right: as a function of the relative error on b/a ($\epsilon(b/a)$). Red contours correspond to values for which there is a 50% and 100% error on b/a.

As a first step, we must select a sample based on relevant criteria. This is meant to ensure that we have reliable morphological and kinematical parameters and to reduce statistical errors. Given that any kinematical modelling relies on prior morphological information (galaxy centre, ellipticity, PA), we can only use a combination of values derived from spectral fitting, for instance the SNR, and from morphological modelling such as a measure of a galaxy radius to select our sample.

Before this internship, spectral fitting on the integrated spectra of the galaxies had already been done, and we combined our data with morphological information from COS-MOS catalogues as discussed in the previous section. Potentially useful morphological information included half-light radii, magnitudes, ratios of minor to major axis (b/a) or equivalently a measure of the ellipticity of the galaxies. Nevertheless, using this data without checking first how well it compares to values found in other catalogues and/or derived using different softwares/models could lead to high biases and uncontrolled errors. Thus, before discussing any selection criteria for our sample, we must first assess the reliability of the parameters we are going to use in later sections.

Important values to check are the half-light radius, as it will be used to select our sample, the b/a ratio and the PA since these are prior information for the kinematical modelling. We also checked that there was a correlation between GALFIT and the catalogues magnitudes. The axes ratio has a crucial importance since it is directly related to the inclination of the galaxy on the sky through Eq. 1. Given a certain error $\Delta(b/a)$, and using the usual formula for computing the error $\Delta f = |\partial_x f|\Delta x$ of a function f, we find for the inclination

$$\Delta i = \Delta(b/a) \left| \frac{b}{a} \left(2 - \frac{b}{a} \right) \right|^{-1/2} \tag{4}$$

This is illustrated in Fig. 1 where Δi has been plotted as a function of b/a and its error (absolute on the left, relative on the right). Contours of the error on b/a have been over-plotted to show how evolves Δi given a fixed error on b/a. As expected, the higher the error on b/a the higher the error on i. An error as high as 50% could yield $\Delta i \approx 27°$, though this value is reached for $b/a \approx 1$ where the axes ratio is the least constrained by the morphology. A more appropriate error on b/a of 20% gives a maximum Δi slightly above 10°, which is correct.

Since the inclination has a strong impact on the galaxy intrinsic maximum rotational velocity, and potentially on the classification of galaxies as rotationnaly supported or dispersion dominated, this indicates us that for any proper kinematical modelling we must check carefully that the values of axes ratios are consistent between catalogues.

2.4.2   Catalogues used for comparison

As stated in previous sections, we cross-matched our catalogue of galaxies detected by MUSE in COSMOS with Cassata's and Tasca's, two tables with morphological information for the galaxies listed in Laigle et al. (2016). However, as can be seen in Fig. 5 and 4, we found large discrepancies between the parameters. Thus, to better understand their origin, we chose to cross-match our catalogue with another one also based on Laigle catalogue. This table has fewer HST counterparts of MUSE galaxies than in the other two but it contains additional morphological information which we can use for the comparison. In addition to that, we already had GALFIT morphological information on ~ 500 group galaxies with strong confidence in their value. Therefore, we chose to compare the data in the three morphological catalogues with that of GALFIT.

2.4.3   Total magnitudes

The first value we can easily compare is the apparent magnitude. Cassata's, Tasca's and Zurich's catalogues provide a measure of the total magnitude derived from fitting with SExtractor a single Sérsic profile with a free Sérsic index n on HST images.
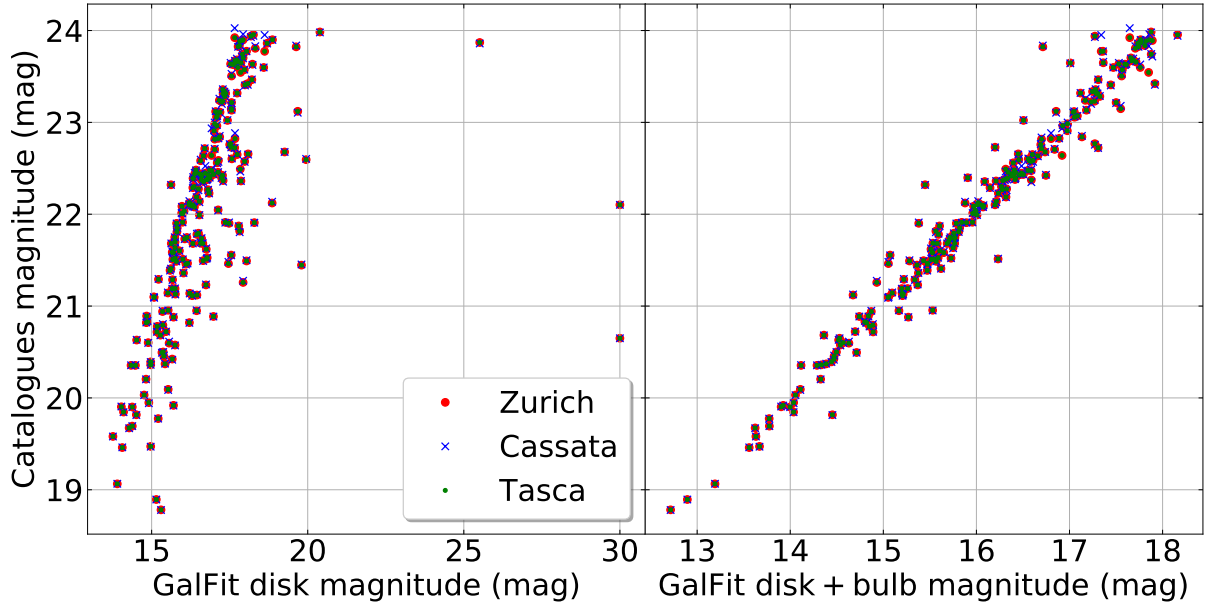
Figure 2: Comparison between the morphological catalogues magnitudes and that of GALFIT for cluster galaxies. Magnitudes from the catalogues agree well between each other. Left: compared with GALFIT disk magnitude only. The slope is too high and a few points are scattered far from the line. Right: compared with the total GALFIT magnitude as defined in Eq. 7. We find a linear relation with a scatter of about 1.6 mag.

Given that GALFIT galaxies light profile was modelled using two Sérsic profiles with fixed Sérsic indices ($n = 1, 4$), we have two measures of their magnitude: one for the bulge component $m_{\mathrm{b}}^{\mathrm{GF}}$, and another for the disk component $m_{\mathrm{d}}^{\mathrm{GF}}$. To have a meaningful comparison between magnitudes, we need to compute the GALFIT total magnitude by combining the bulge and the disk components. Both are defined as

$$m_i^{GF} = -2.5 \log_{10}\left(F_i^{\mathrm{GF}}\right) + \mathrm{C} \tag{5}$$

where $i = \mathrm{b, d}$ represents either the bulge or the disk, $F = L/4\pi D^2$ is the flux of the galaxy in some band, L its intrinsic luminosity, D its cosmological luminosity distance to us and C a constant depending on the band used.

Considering that the two components have different luminosities but are located at the same distance, we can add the fluxes together. Thus the total GALFIT magnitude can also be written as

$$m_{\mathrm{tot}}^{\mathrm{GF}} = -2.5 \log_{10}\left(F_{\mathrm{b}}^{\mathrm{GF}} + F_{\mathrm{d}}^{\mathrm{GF}}\right) + \mathrm{C} \tag{6}$$

Inverting Eq. 5 to get the components flux as a function of their magnitude and inserting it into Eq. 6 yields

$$m_{\mathrm{tot}}^{\mathrm{GF}} = -2.5 \log_{10}\left[10^{-\frac{m_{\mathrm{b}}}{2.5}} + 10^{-\frac{m_{\mathrm{d}}}{2.5}}\right] \tag{7}$$

This is the value that should be compared with the three catalogues magnitudes. Fig. 2 shows how these scale with each other and with GALFIT disk magnitude on the left, and the total magnitude from Eq. 7 on the right. As expected, the catalogues give the same value except for a few points. We see that the total GALFIT magnitude gives a much better, poorly scattered linear relation with the catalogues magnitudes. Even though there is an offset between GALFIT and the catalogues, this is due to using different conventions for the constant term in Eq. 5.

The same comparison was done on field galaxies, except we did not have GALFIT magnitudes in this case. We also found a good agreement between the catalogues magnitudes.

2.4.4   Morphological type classification

We might expect to have some discrepancies in our data because of the models used between GALFIT and SExtractor/GIM2D. A way to check this effect is to study how these differences scale with the morphological type of the galaxies. For instance, if we use the disk half-light radius of GALFIT to compare with that of SExtractor, we might expect to have some scatter in our relation for the elliptical galaxies as the disk component is not the best one to describe them.

To see how these relations scale with morphological types, we can use the classification given in the three morphological catalogues. These classifications are based on methods which can be quite different and which can use

Figure 3: Comparison between morphological types given in Tasca and Zurich catalogues against that of Cassata. Galaxies are labelled as follows: E for ellipticals, Sp for spirals/disks-like, Irr for irregulars. The percentage of galaxies falling into the given classes is indicated in red and the method compared with Cassata's is shown on the top left corner of each plot. We find good agreement between Tasca and Cassata types but not between Cassata and Zurich.

morphological parameters in different ways. A more detailed explanation of the parameters used, of how these methods work, of their strength and weaknesses can be found in
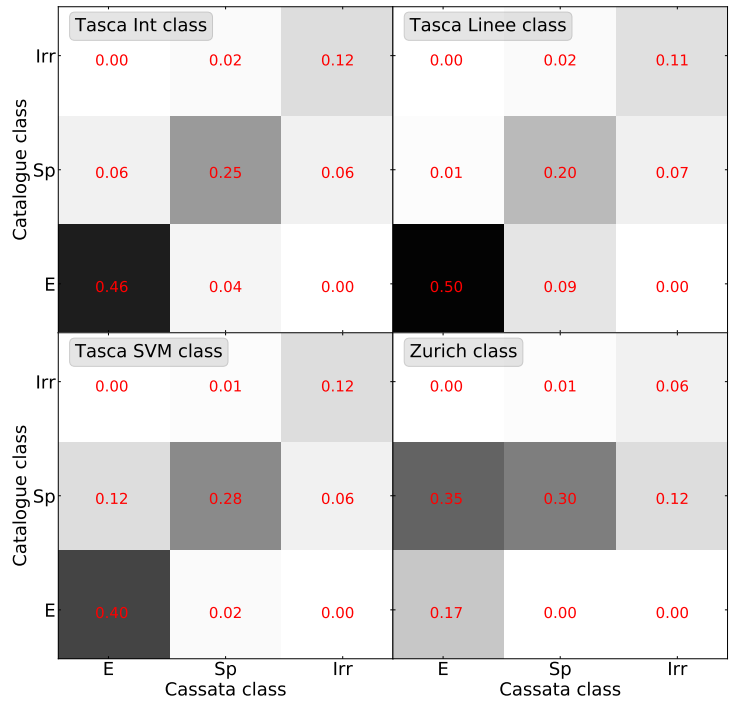
Appendix A. We provide below a short introduction to these classifications:

- Cassata's catalogue gives a classification based on morphological parameters they derived with SExtractor. To do so, they use a reference of 500 galaxies with known parameters which they visually classify as either elliptical, disk-like/spiral or irregular. From this set, each time a new galaxy must be classified, its 11 closest neighbours are inspected and the most frequent class is assigned to the galaxy.

- Tasca's catalogue gives different classifications based on three methods. The first one is similar to the one used by Cassata. This is also the classification they recommend to use because this is the one they put the more their trust in. The second one uses the technique described in (insert Abraham 1996 here) using the asymmetry and concentration parameters. The last one uses a support vector machine to classify galaxies.

- Zurich's catalogue gives a single classification called Zurich Estimator of Structural Type (ZEST) which is described in (Scarlata et al., 2007). This method is based on a Principal Component Analysis (PCA). They decided to keep the first three Principal Components (PA) which retain most of the information present in the original five parameters (concentration, asymmetry, Gini coefficient, second-order moment of the brightest pixels producing 20% of the total flux and the ellipticity of the galaxy).

The morphological types given in Tasca's and Zurich's catalogues are compared against the class given by Cassata in Fig. 3. We observe a good agreement between Cassata's and Tasca's types with just a few elliptical galaxies labelled as disk-like and vice versa. Roughly 50% of the galaxies appear to be elliptical. On the contrary, Zurich's classification seems to label more than 70% of the galaxies as disk-like, including a large number of elliptical galaxies .

Considering the recommendation of Tasca to use its Int class and since we find a good agreement between Cassata's morphological type and those given by Tasca, we decided to use and to stick to Cassata's class throughout this work whenever we needed to separate galaxies between elliptical/disk-like/irregulars. This choice also ensured us to have the largest sample possible with a coherent classification as Cassata's catalogue is the one with the largest number of HST counterparts of MUSE galaxies in the COSMOS field. Because of the incompatible results between Zurich's and Cassata's/Tasca's types, we decided to put aside these values and not use them, though this shall require further investigation in future work to assess the origin of these discrepancies.
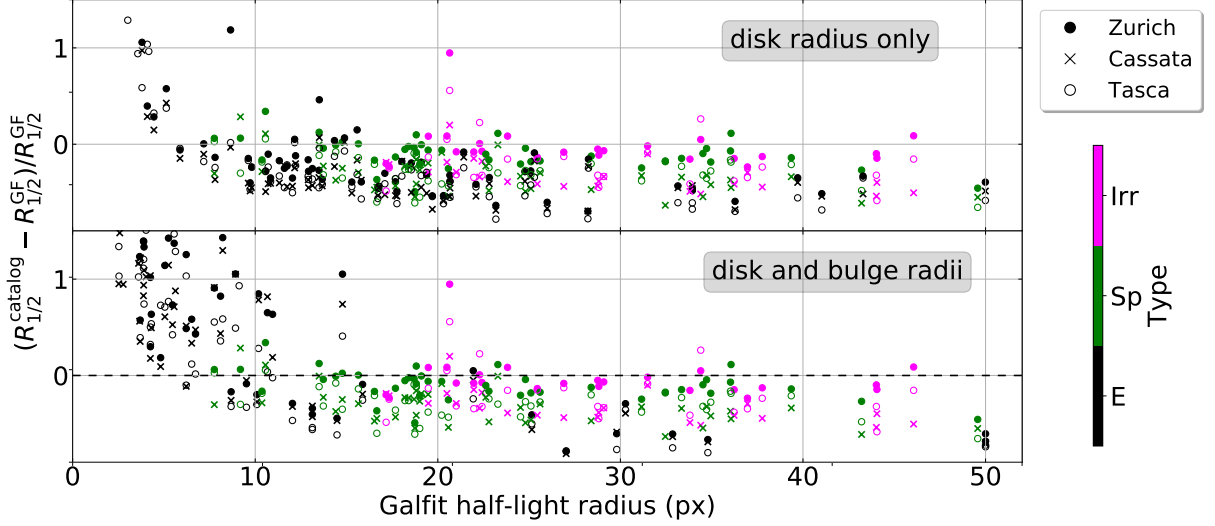
Figure 4: Relative error on the half-light radius between the catalogues and GALFIT. Points have been colour coded according to their classification given in Cassata's catalogue (Irr for irregular, Sp for spiral/disk, E for ellipticals). Top: GALFIT disk radius is used for all the points. We observe an underestimation of the catalogues radius with respect to that of GALFIT for elliptical galaxies. Bottom: same plot with GALFIT bulge radius used for elliptical galaxies. In this case, we find an overestimation of the radius.
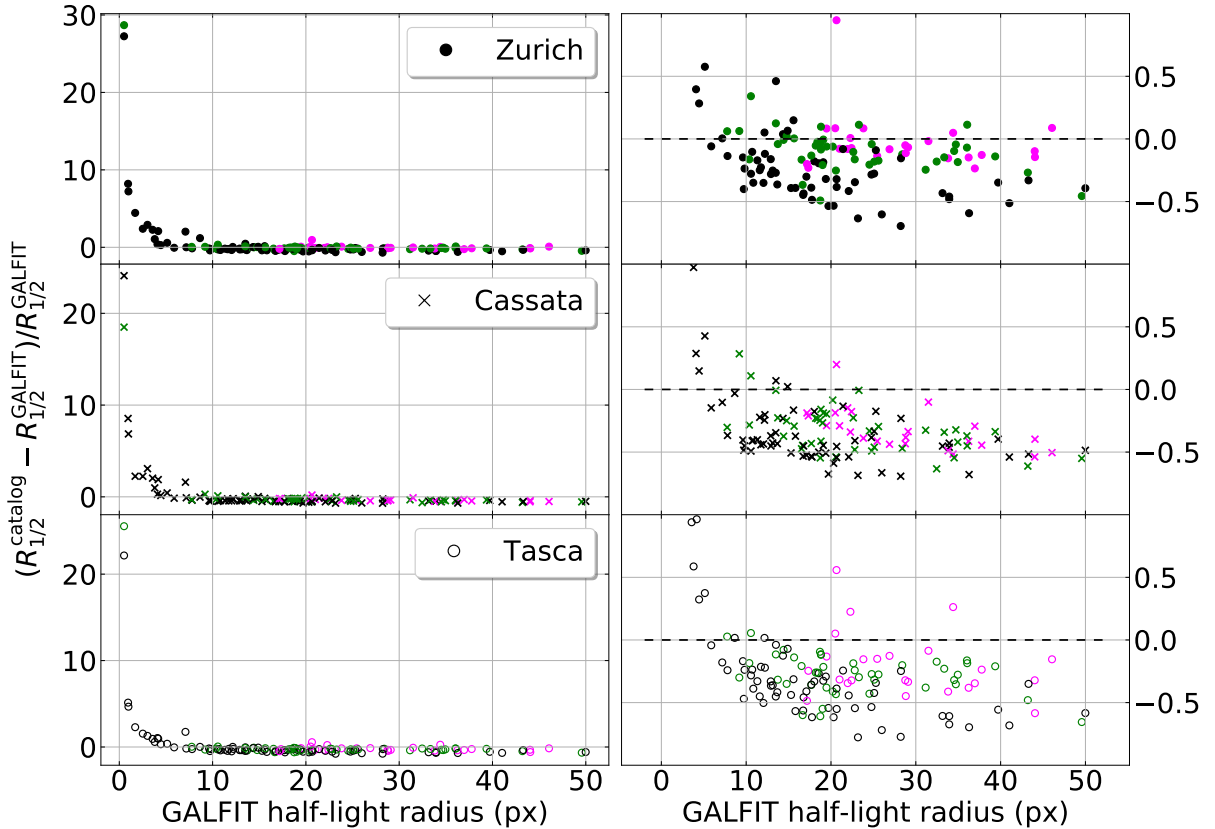

Figure 5: Comparison between half-light radii from the morphological catalogues and the radius of GALFIT disk component. This plot is similar to Fig. 4 top plot but each catalogue was separated in its own subplot. Left: full range of relative error. Right: a zoom on the points with $R_{1/2}^{GF} \geq 5\,\mathrm{px}$.

2.4.5   Half-light radii

Perhaps the most important parameter we have to check is the half-light radius. Indeed, if we underestimate it, we might remove from our sample resolved galaxies and therefore reduce our statistics. On the other hand, overestimating it would give us too many unresolved galaxies for which we would spend time removing noise dominated pixels without being able to perform their kinematical analysis in the end. Hence, it is mandatory to thoroughly check the values of the half-light radius from the three catalogues against that of GALFIT, and understand the origin of any discrepancies if there happens to be some.

We found a quite large disagreement between GALFIT half-light radius and those given in the morphological catalogues, as well as between them. This is illustrated in Fig. 4 and 5 where half-light radii in the catalogues are compared against that of GAL-FIT. Galaxies are colour coded according to the classification given in Cassata's catalogue. We checked that using Tasca's classifications as described in Sec. 2.4.4 did not change our conclusions. In these plots, we decided to use for the x-axis the half-light radius of the GALFIT disk component $R_{1/2,\mathrm{d}}^{\mathrm{GF}}$ for all the galaxies, even though we might expect the ellipticals to be better described by their GALFIT bulge half-light radius. This choice is further discussed below.

The catalogues radii seem to be overestimated with respect to that of GALFIT for low $R_{1/2,\mathrm{d}}^{\mathrm{GF}}$. These are computed with SExtractor and, given that it does not take into account the PSF in its fitting routine, we expect the PSF to dominate for galaxies with small angular sizes. On the contrary, GALFIT does take into account the PSF in its calculation, and therefore we expect its half-light radius to decrease with lower values of $R_{1/2,\mathrm{d}}^{\mathrm{GF}}$.

When focussing on galaxies with a GALFIT radius larger than the HST-ACS PSF FWHM which is around 0.15" $(4-5\,\mathrm{px})$, we observe a global underestimation for all the catalogues, up to roughly 50%. This scatter is mainly due to elliptical galaxies. On the contrary, radii of disk-like galaxies have the least scatter and biais, especially the values given in Zurich's catalogue. This different behaviour between elliptical and disk-like galaxies might be explained, as mentioned above, by the fact we are using the half-light radius of GALFIT disk component to asses the reliability of the elliptical galaxies radii give in the catalogues. A better choice may be to use the bulge component, which better describes the light profile of an elliptical galaxy, and its half-light radius for this population.

If we decide to split the galaxies into two categories, ellipticals and disks/irregulars, and if we use for the first category the bulge radius $R_{1/2,\mathrm{b}}^{\mathrm{GF}}$, and for the second $R_{1/2,\mathrm{d}}^{\mathrm{GF}}$, we

find that elliptical galaxies half-light radii from the catalogues are now overestimated as shown in Fig. 4 lower panel. These results suggest that elliptical galaxies in this sample are neither dominated (in terms of radius) by the disk component, nor by the bulge in the GALFIT model. Even though we did not push further the analysis on this discrepancy, we still mention that the next step should be to directly compute the half-light radius of the GALFIT model by integrating Eq. 3 up to half its total luminosity.
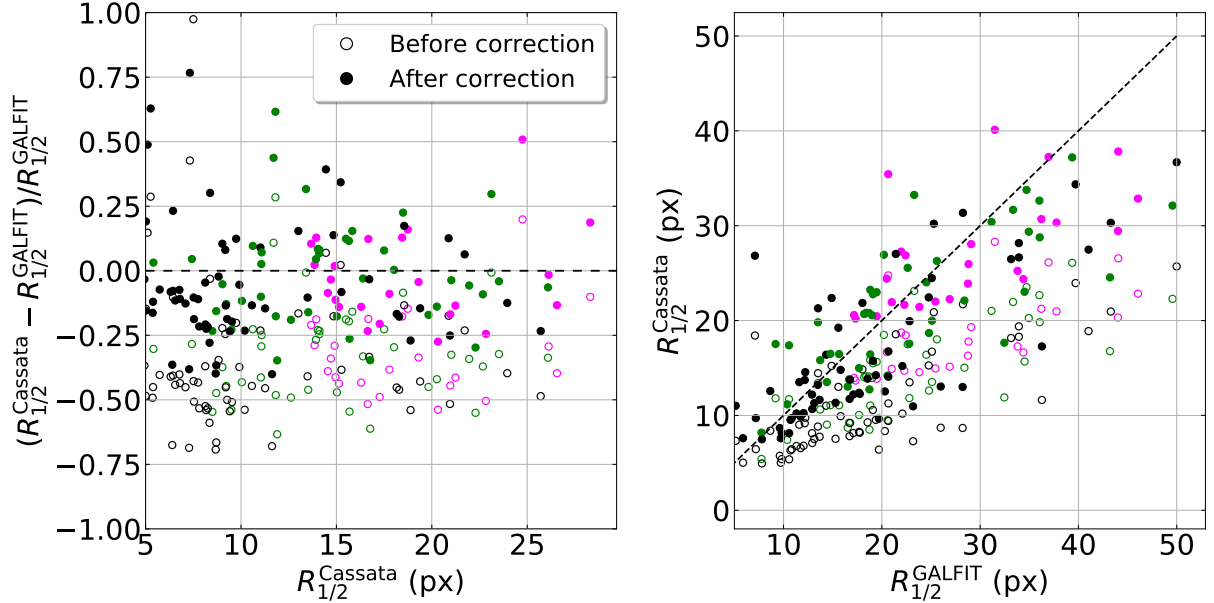

Figure 6: Biais and scatter before and after applying the correction mentioned in the paragraph. Left: half-light radius relative error as a function of Cassata's radius. Right: scaling between Cassata's and GALFIT radii. The scatter around 0.2 px is not significantly changed after the bias correction.

Based on Fig. 5, we decided to use the galaxies half-light radii given in Zurich catalogue, keeping in mind that we might have a non-negligible fraction of elliptical galaxies for which their value may be underestimated. However, this is the catalogue with least HST counterparts. Thus, in order to increase our sample, we also chose to select additional galaxies found in Cassata's catalogue but not in Zurich's. As it seems that Cassata's radius is more bias than Zurich's, we fitted a linear relation onto the relative error data, which translates as

$$R_{1/2}^{\text{Corrected}} = R_{1/2}^{\text{Cassata}} \left(1 + \beta + \alpha R_{1/2}^{\text{Cassata}}\right)^{-1} \tag{8}$$

where $R_{1/2}^{\text{Corrected}}$ is the new half-light radius after the bias correction and α, β the parameters of our fit. Based on previous arguments, we only fitted galaxies for which $R_{1/2}^{\text{GF}} > 5\,\text{px}$. Once a best fit solution was found, we slightly adjusted it by applying weights on ellipticals in order to limit their impact on disk-like galaxies radii which appeared to be too much overestimated. We used $\alpha \approx 1.95 \times 10^{-3}$ and $\beta = -0.349$.
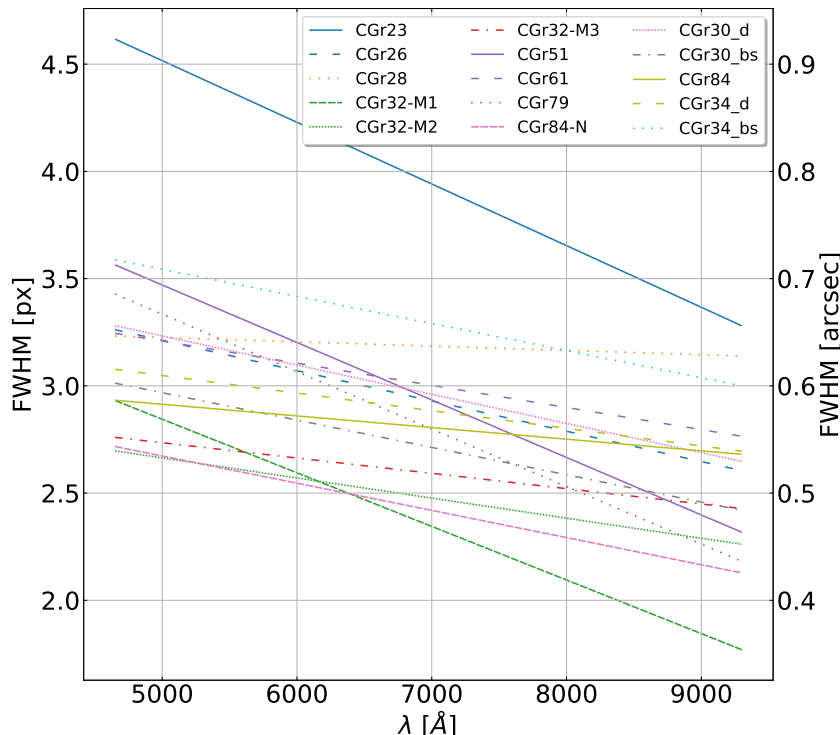
Figure 7: PSF FWHM variation with wavelength for the 13 FoVs as measured by Valentina. At least two values of the FWHM were derived from stars in the FoVs by fitting a Moffat distribution to their light profile. We assumed a linear evolution with wavelength. Strong fluctuations appear depending on the observed FoV.

2.5   SNR and size selection

2.5.1   Size selection

Since we are interested in keeping well resolved field galaxies, we need to apply relevant criteria in order to select the right galaxies. The most obvious parameter we can use to make our selection is the size of the galaxy. We already checked in Section 2.4.5 biases which might arise and their origins, and we corrected them whenever possible. Thus, we only need to define a size criterion to select our sample.

Following the earlier work done in Bacon et al. (2015) and Bacon et al. (2017), the MUSE Point Spread Function (PSF), that is the pattern we obtain when we observe a point-like source with MUSE, is most well described by a Moffat (1969) profile

$$I_{\mathrm{PSF}}(r) = I_0(1 + (r/\alpha)^2)^{-\beta} \tag{9}$$

where r is the radial distance to the centre and α, β are two seeing dependant parameters. In our case, we are interested in the Full Width at Half Maximum (FWHM) since it is directly related to the seeing conditions and since it gives us information about the minimum spatial extent within which we start to loose information. The FWHM can be

19

easily derived from the equality $I_{\mathrm{PSF}}(\mathrm{FWHM}/2) = \mathrm{I_0}/2$ using Eq. 9, from which we get the following relation

$$\mathrm{FWHM} = 2\alpha\sqrt{2^{1/\beta} - 1} \tag{10}$$

According to the aforementioned articles the value of β is expected to remain roughly constant and, additionally, we would expect from differential image motion theory (insert this paper here when read 10.1086/342683) the FWHM to linearly decrease with wavelength.

All galaxies are observed via their [OII] doublet at the same rest-frame wavelength. But, given that they are all field galaxies located at a different redshift z, we actually observe them at wavelengths covering the entire MUSE spectrum, that is we have the usual relation

$$\lambda_{\mathrm{obs}} = \lambda_{\mathrm{em}}(1 + z) \tag{11}$$

where λ_{em}, λ_{obs} are respectively the emitted (rest-frame) and observed wavelengths. Therefore, there is not only one FWHM value per field (the FWHM will also vary with MUSE fields as seeing conditions change from date to date), but one per galaxy, which we can derive if we know the two parameters (slope and offset) which characterise the linear evolution of the FWHM with wavelength. To derive this relation, we need at least two measures of the FWHM at two different wavelengths per field. Assuming seeing conditions are similar within a field (no spatial dependence), we can use the same linear relation per MUSE field to compute the FWHM for the [OII] wavelength at the redshift of the galaxy.

As discussed above, β should remain constant, which means the FWHM is entirely described by the parameter α through Eq. 10. The measure of α had already been done by V. Abril-Melgarejo on at least two stars per field. For each star, two measures of α were computed by fitting a Moffat profile onto their [OII] and [OIII] images at the redshift of the observed structure (see Table 1).

Though a more rigorous modelling of the wavelength variation of the PSF FWHM including both more data points and potentially higher order terms is mandatory for future analysis, we decided to stick to this values in the present work, keeping in mind the large uncertainties which will affect the velocity dispersion maps in the modelling section. A representation of the FWHM variation with wavelength for the 16 observations is shown in Fig. 7. Most MUSE fields have FWHM values below 0.7" which is not surprising given that it was one of the constraints of the observations. CGr23 is the only FoV to have its FWHM above 0.7" for almost every wavelength. Only galaxies further than $z \approx 1.11$. In Table. 1, the seeing is the average over the OBs for the [OII] doublet at the redshift of the group which is around 1.17. Hence the value below 0.7".

Considering that the FWHM is a measure of how spread a point-like source is, and since we are interested in working with resolved enough galaxies in order to better constrain their kinematics, we would like galaxies to have a characteristic size at least above the FWHM. Given that for almost all the fields we have an upper limit on the FWHM of about 0.7", we decided to use this upper limit as our size selection criterion

$$R_{1/2} \geq 0.35" \approx \text{FWHM}/2 \tag{12}$$

Moreover, according to Swinbank et al. (2017) who compared the half-light radius of the nebular [OII] emission in MUSE images with that of their HST counterpart in ACS *I* or WFC3 *H*-band, the [OII] half-light radius seems to scale with the HST radius as

$$R_{1/2}^{\text{OII}} = (1.18 \pm 0.03)R_{1/2}^{\text{HST}} \tag{13}$$

Thus, we expect the galaxies in the MUSE images to be larger than their HST counterparts, which means our choice of lower limit for the morphological radius in our sample should eliminate most of the unresolved galaxies. Though, we also risk to eliminate resolved galaxies in our selection.

2.5.2   SNR selection

The other information we can use to select our sample is the Signal to Noise Ratio (SNR), which tells us how well our galaxy is detached from the background. The SNR is generally derived as the ratio between the source's signal and the background level. The noisier an image, the lower the SNR is.

As explained in later sections, the galaxies must be automatically and then manually cleaned before fitting a kinematical model on the velocity maps in order to remove any pixel dominated by noise which might compromise the fit. One of the criteria used by the routine to decide whether a pixel belongs to the galaxy is a lower limit on the SNR of pixel (typically 5). Thus, if we want to have enough detection in our cleaned maps to perform the kinematical modelling, we must select galaxies with a strong enough SNR.

In our case, PLATEFIT, described in), was run on the integrated spectrum of the galaxies in order to derive their spectral features. From the parameters returned by CAMEL, we used the [OII] flux and its error to derive the SNR as

$$\text{SNR} = \frac{[\text{OII}] \text{ flux}}{[\text{OII}] \text{ flux error}} \tag{14}$$

This is the [OII] SNR from the integrated galaxy spectrum computed using pixels within data cubes restricted around the galaxy. Since the typical SNR value used by the routine to clean the maps is around 5, we decided as a first step to choose an SNR lower
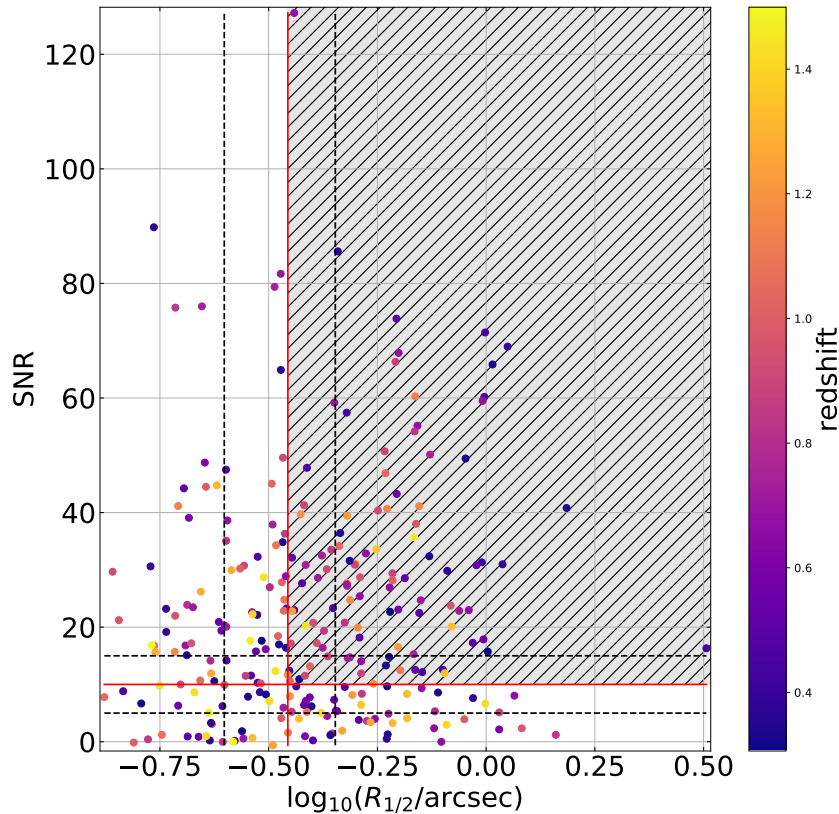
Figure 8: Full sample of 261 field galaxies with our selection box over-plotted (hatched area). Galaxies with $5 \leq \mathrm{SNR} \leq 15$ and $0.25" \leq R_{1/2} \leq 0.45"$ (bounds plotted as dashed lines) were visually inspected to check how many resolved galaxies we might have lost. Selection criteria from Sec. 2.5 are also plotted as solid red lines. No specific trend appear with redshift.

limit of 10, allowing us to keep galaxies with strong enough detection after the automatic cleaning is performed.

2.6 Characterisation of the sample

2.6.1 Selecting galaxies

We decided to visually inspect galaxies around the SNR and the size cuts to quantify (a) how many resolved galaxies would be lost if we applied the criteria given in Sec. 2.5.1 and 2.5.2 (false negative) (b) how many unresolved galaxies would be selected in our sample (false positive). To do so, we defined four boxes: $5 \leq \mathrm{SNR} \leq 10$, $10 \leq \mathrm{SNR} \leq 15$, $0.25" \leq R_{1/2} \leq 0.35"$ and $0.35" \leq R_{1/2} \leq 0.45"$ containing respectively 46, 20, 58 and 49 galaxies. We then ran the automatic cleaning routine on all the galaxies in these boxes. After visually inspecting their size in the cleaned maps, we classified them as resolved or not. These boxes and the SNR, half-light radius and redshift of the full sample of field galaxies before selection are shown in Fig.8.

Among the 261 field galaxies, 103 fall into the limits imposed in Sec. 2.5. We find that roughly 26% of the galaxies below the cuts are actually false negatives and that 15% above them are false positives. Since this classification is purely visual, slightly relaxing the constraints on when a galaxy is resolved or not allow these values to vary by roughly 10%. Hence, it seems our choice of lower bounds for the SNR and the half-light radius is fine, though in future works we might increase our sample by a factor of ~ 1.5.

2.6.2   Redshift distribution

The choice of the [OII] $\lambda\lambda 3729, 3729$ Å doublet for the kinematical analysis was due in part to the large range of redshift it covered given the MUSE observed wavelengths. We therefore had in our catalogue galaxies spanning a redshift range from 0.3 to about 1.4. As show in Fig. 9, after our selection we loose the majority of the most distant galaxies as well as a significant fraction of galaxies with z around 0.3, 0.5 and 0.75. Globally, we are selecting less galaxies per redshift bin than we are putting aside. The average and median redshifts are 0.749 and 0.719 for the selected galaxies, 0.809 and 0.750 for the unselected ones. Thus, our sample remains consistent in terms of redshift even after performing the SNR and size selections.

2.6.3   Mass-SFR relation
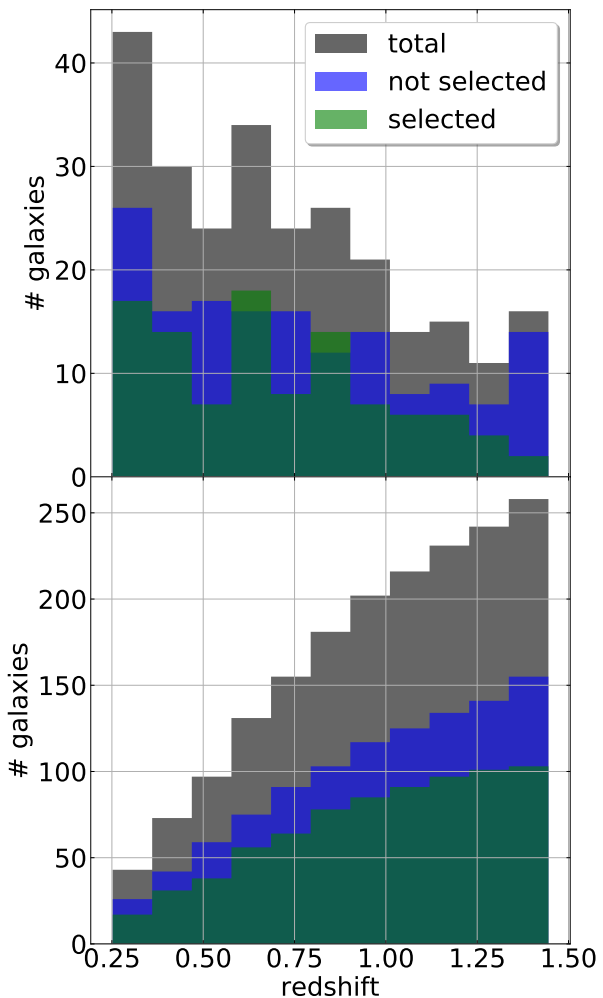

Figure 9: Redshift distribution of the total sample (grey), selected (green) and unselected (blue) galaxies. Redshift bins of size 0.1 have been used. Top: density plot as a function of redshift. Bottom: cumulative distribution. We lack most of the galaxies at redshift 1.4. Other redshift bins do not loose to many galaxies with respect to the unselected ones except maybe at $z \approx 0.5$.

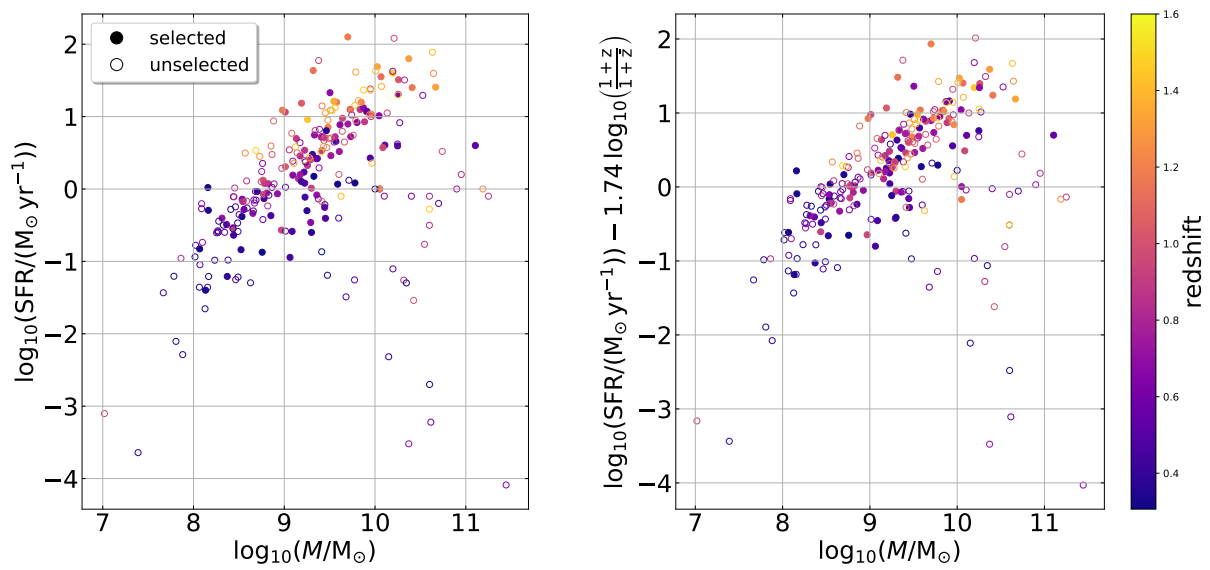Figure 10: SFR-mass relation for selected (filled circles) and unselected (open circles) galaxies. Left: SFR extracted from the morphological catalogues. Right: the redshift corrected SFR as given in Eq. **??**. We obtain the usual main sequence of galaxies as a linear relation between SFR and mass (in log-log space), as well as quenched galaxies on the lower right part of the plane which are removed when performing the selection.

3 Kinematical modelling

3.1 Cleaning

Before trying to fit a model onto the velocity maps to derive the kinematical parameters of our galaxies, we need to remove any pixel which might be dominated by the noise. Such a cleaning is generally done by keeping pixels whose [OII] $\lambda\lambda 3729, 3729\,\text{Å}$ doublet emission line is visually identifiable with respect to the continuum. This quite subjective procedure can be objectified by considering the SNR of each pixel, which is computed in the MUSE pipeline, and by keeping those whose value is above a certain threshold which we chose to be 5.

However, in some cases, we expect to find a strong continuum emission which we may over-interpret as a spectral feature such as [OII]. Continuum emission comes from various physical processes, most being independent from the others, which implies a larger dispersion in the pixels spectra than in the [OII] case. The dispersion threshold above which we consider pixels are noise dominated will depend on the galaxy redshift. Indeed, considering Gaussian line profiles, we find the spectral dispersion as a function of the LSF FWHM of the line by solving $\exp\left\{-(\text{FWHM}/2)^2/(2\sigma^2)\right\} = 1/2$, i.e.

$$\sigma(z) = \frac{\text{FWHM}}{2\sqrt{2\log 2}} \tag{15}$$

We can explicitly express the redshift dependence by defining an equivalent velocity dispersion σ_v as

$$\frac{\sigma}{\lambda_\text{em}(1+z)} = \frac{\sigma_\text{v}}{c} \tag{16}$$

This value defines the usual velocity dispersion we expect to measure from the emission line of a galaxy at redshift z. As the Universe expands (z going from ∞ to 0), its bulk motion takes over the local movement of matter, reducing the observed dispersion. We decided to choose a velocity dispersion threshold of $0.8\sigma_\text{v}$ for all the galaxies throughout this work.

The cleaning was automatically performed with a routine using both thresholds defined above. Cleaned maps were produced and the velocity maps were visually inspected. Isolated pixels were removed even if they had a clearly visible [OII] doublet. Twelve galaxies were unresolved and 3 were too close to the edges which resulted in missing data. Relaxing the SNR threshold to 3 and removing any pixels on the edges of the galaxies with too weak [OII] emission lines allowed us to recover 6 galaxies out of 12. In the case of resolved galaxies, we also inspected their [OII] doublet near the edges and we removed any pixel whose velocity seemed inconsistent with that of its neighbours (a single negative value around positives ones for instance).

3.2   Kinematical parametrisation

The velocity maps we had from the MUSE pipeline only give us information on a fraction of the velocity. Indeed, the velocity of a given pixel is computed using the well known Doppler effect which will redshift pixels going away from us and blueshift those approaching, i.e.

$$\frac{\lambda_{\text{obs}} - \lambda_{\text{em}}}{\lambda_{\text{em}}} = \frac{v}{c} \tag{17}$$

with v positive if it recedes from us and negative if it approaches. Special relativistic effects being negligible in this case, it means the only measure we have is the radial component of the gas velocity within the pixels. Depending on the basis we choose to decompose our velocity vector, this component will be written differently. In our case, we will use the coordinate system defined in ? (?). Using cylindrical coordinates relative to the galactic plane, we can write the observed projected radial component as

$$V_{\text{obs}}(R, \theta, i, V_{\text{sys}}, \text{PA}) = V_{\text{sys}} + (V_{\text{rot}}(R) \cos\theta + V_{\text{exp}}(R) \sin\theta) \sin i + V_z(R) \cos i \tag{18}$$

where V_{obs}, V_{sys}, V_{rot}, V_{exp} and V_z are the observed, systematic, rotational, expansion and vertical components of the velocity respectively. In practice, spectroscopic measurements give us $\Delta V_{\text{obs}} = V_{\text{obs}} - V_{\text{sys}}$. In Eq. 18, the dependence on the major axis (kinematical) position angle is implicit as θ is defined as the angle in the galactic plane starting from the major axis. Thus, $\theta = 0°$ (90°) when we measure the velocity of a point on the major (minor) axis. The dependence of V_{obs} with the radial distance R to the centre of the galaxy also makes implicit its dependence on the galaxy centre position.

A representation and the definitions of the coordinate system, angles and vector decomposition can be found in Appendix **??**. Both R, θ and the galaxy centre $(x_{\text{c}}, y_{\text{c}})$ can be derived from the images, but the inclination of the galaxy must be know in advance. As it will be explained later, models poorly converge when the inclination is let free to vary. Hence, it must be used as a fixed input. More importantly, assuming the rotation curve along the major axis reaches a maximum rotational velocity or at least a plateau, as should be the case in dark matter dominated galaxies (ref here), we see from Eq. 18 that the maximum rotational velocity will scale as

$$V_{\text{obs}}^{\text{max}}(R_{\text{max}}, i) = V_{\text{rot}}(R_{\text{max}}) \sin i \tag{19}$$

where R_{max} represents the radius at which the maximum velocity or the plateau is reached. Thus, just by looking at the rotation curve and by measuring its maximum value, we cannot raise the degeneracy between the inclination, which will lower the velocity, and the real one . This explains the care taken in checking prior information we had on the b/a ratio from which is computed the galaxy inclination.

3.3   Model

Given the smooth cleaned velocity maps, we can deduce the kinematical parameters of our galaxies by fitting 2D velocity models. Many can be used, but we describe here the one we utilised in this work. We used a parametric model relying on the assumption of a thin disk. This is no longer the case when galaxies are seen nearly edge-on ($75° \lesssim i \lesssim 90°$) due to the increasing depth leading to higher values of opacity. The second assumption is that we can actually model our galaxies with a rotation curve and so that we do not have non-rotational bulk motions. In our case, we assume we have smooth velocity fields with no bar, no arms and no clumps such as HII regions. Nevertheless, based on previous morpho-kinematical studies (ref here), we might expect to find a significant fraction of our galaxies to be dispersion dominated, some with highly perturbed morphologies due to merging in some cases. In our model, 4 morphological and 1 kinematical parameters are used. The inclination of the galaxy, its centre right ascension and declination and the PA of the major axis must be given as fixed values. The kinematical parameter corresponds to the systematic velocity, that is the radial component of the velocity due to the expansion of the Universe.

References

Abraham, R. G., Valdes, F., Yee, H. K. C., & van den Bergh, S. (1994, Sep). The Morphologies of Distant Galaxies. I. an Automated Classification System. *Astrophysical Journal*, *432*, 75. doi: 10.1086/174550

Abraham, R. G., van den Bergh, S., Glazebrook, K., Ellis, R. S., Santiago, B. X., Surma, P., & Griffiths, R. E. (1996, Nov). The Morphologies of Distant Galaxies. II. Classifications from the Hubble Space Telescope Medium Deep Survey. *Astrophysical Journal Supplement*, *107*, 1. doi: 10.1086/192352

Bacon, R., Brinchmann, J., Richard, J., Contini, T., Drake, A., Franx, M., . . . de Zeeuw, T. (2015, Mar). The MUSE 3D view of the Hubble Deep Field South. *Astronomy and Astrophysics*, *575*, A75. doi: 10.1051/0004-6361/201425419

Bacon, R., Conseil, S., Mary, D., Brinchmann, J., Shepherd, M., Akhlaghi, M., . . . Carollo, M. (2017, Nov). The MUSE Hubble Ultra Deep Field Survey. I. Survey description, data reduction, and source detection. *Astronomy and Astrophysics*, *608*, A1. doi: 10.1051/0004-6361/201730833

Bershady, M. A., Jangren, A., & Conselice, C. J. (2000, Jun). Structural and Photometric Classification of Galaxies. I. Calibration Based on a Nearby Galaxy Sample. *The Astronomical Journal*, *119*(6), 2645-2663. doi: 10.1086/301386

Bertin, E., & Arnouts, S. (1996, June). SExtractor: Software for source extraction. *Astronomy and Astrophysics Supplement*, *117*, 393-404. doi: 10.1051/aas:1996164

Conselice, C. J. (1997, Nov). The Symmetry, Color, and Morphology of Galaxies. *Publications of the Astronomical Society of the Pacific*, *109*, 1251-1255. doi: 10.1086/134004

Graham, A. W., Driver, S. P., Petrosian, V., Conselice, C. J., Bershady, M. A., Crawford, S. M., & Goto, T. (2005, Oct). Total Galaxy Magnitudes and Effective Radii from Petrosian Magnitudes and Radii. *The Astronomical Journal*, *130*(4), 1535-1544. doi: 10.1086/444475

Hubble, E. P. (1922, Oct). A general study of diffuse galactic nebulae. *Astrophysical Journal*, *56*, 162-199. doi: 10.1086/142698

Hubble, E. P. (1926, Dec). Extragalactic nebulae. *Astrophysical Journal*, *64*, 321-369. doi: 10.1086/143018

Hubble, E. P. (1929, Jan). A Relation between Distance and Radial Velocity among Extra-Galactic Nebulae. *Contributions from the Mount Wilson Observatory*, *3*, 23-28.

Kent, S. M. (1985, Oct). CCD surface photometry of field galaxies. II. Bulge/disk decompositions. *Astrophysical Journal, Suppl. Ser.*, *59*, 115-159. doi: 10.1086/191066

Knobel, C., Lilly, S. J., Iovino, A., Kovač, K., Bschorr, T. J., Presotto, V., ... Welikala, N. (2012, Jul). The zCOSMOS 20k Group Catalog. *The Astrophysical Journal*, *753*(2), 121. doi: 10.1088/0004-637X/753/2/121

Knobel, C., Lilly, S. J., Iovino, A., Porciani, C., Kovač, K., Cucciati, O., ... Scaramella, R. (2009, Jun). An Optical Group Catalog to z = 1 from the zCOSMOS 10 k Sample. *The Astrophysical Journal*, *697*(2), 1842-1860. doi: 10.1088/0004-637X/697/2/1842

Laigle, C., McCracken, H. J., Ilbert, O., Hsieh, B. C., Davidzon, I., Capak, P., ... Zabl, J. (2016, June). THE COSMOS2015 CATALOG: EXPLORING THE 1 < *z* < 6 UNIVERSE WITH HALF A MILLION GALAXIES. *The Astrophysical Journal Supplement Series*, *224*(2), 24. Retrieved 2019-03-21, from `http://stacks.iop.org/0067-0049/224/i=2/a=24?key=crossref.13400bd5b9499f45ce2b1d44c4a48475` doi: 10.3847/0067-0049/224/2/24

Lotz, J. M., Primack, J., & Madau, P. (2004, Jul). A New Nonparametric Approach to Galaxy Morphological Classification. *The Astronomical Journal*, *128*(1), 163-182. doi: 10.1086/421849

Moffat, A. F. J. (1969, December). A Theoretical Investigation of Focal Stellar Images in the Photographic Emulsion and Application to Photographic Photometry. *Astronomy and Astrophysics*, *3*, 455.

Peng, C. Y., Ho, L. C., Impey, C. D., & Rix, H.-W. (2002, July). Detailed Structural Decomposition of Galaxy Images. *The Astronomical Journal*, *124*, 266-293. doi: 10.1086/340952

Perlmutter, S., Aldering, G., Goldhaber, G., Knop, R. A., Nugent, P., Castro, P. G., ... Project, T. S. C. (1999, Jun). Measurements of Ω and Λ from 42 High-Redshift Supernovae. *The Astrophysical Journal*, *517*(2), 565-586. doi: 10.1086/307221

Riess, A. G., Filippenko, A. V., Challis, P., Clocchiatti, A., Diercks, A., Garnavich, P. M., ... Tonry, J. (1998, Sep). Observational Evidence from Supernovae for an Accelerating Universe and a Cosmological Constant. *The Astrophysical Journal*, *116*(3), 1009-1038. doi: 10.1086/300499

Rubin, V. C., Ford, J., W. K., & Thonnard, N. (1978, Nov). Extended rotation curves of high-luminosity spiral galaxies. IV. Systematic dynamical properties, Sa -> Sc. *Astrophysical Journal*, *225*, L107-L111. doi: 10.1086/182804

Rubin, V. C., & Ford, J., W. Kent. (1970, Feb). Rotation of the Andromeda Nebula from a Spectroscopic Survey of Emission Regions. *Astrophysical Journal*, *159*, 379. doi: 10.1086/150317

Scarlata, C., Carollo, C. M., Lilly, S., Sargent, M. T., Feldmann, R., Kampczyk, P., ... Takahashi, M. (2007, Sep). COSMOS Morphological Classification with the Zurich Estimator of Structural Types (ZEST) and the Evolution Since z = 1 of the Luminosity Function of Early, Disk, and Irregular Galaxies. *The Astrophysical Journal Supplement Series*, *172*(1), 406-433. doi: 10.1086/516582

Schade, D., Lilly, S. J., Crampton, D., Hammer, F., Le Fevre, O., & Tresse, L. (1995, Sep). Canada-France Redshift Survey: Hubble Space Telescope Imaging of High-Redshift Field Galaxies. *Astrophysical Journal Letters*, *451*, L1. doi: 10.1086/309677

Scoville, N., Aussel, H., Brusa, M., Capak, P., Carollo, C. M., Elvis, M., ... Tyson, N. D. (2007, Sep). The Cosmic Evolution Survey (COSMOS): Overview. *The Astrophysical Journal Supplement Series*, *172*(1), 1-8. doi: 10.1086/516585

Sérsic, J. L. (1963). Influence of the atmospheric and instrumental dispersion on the brightness distribution in a galaxy. *Boletin de la Asociacion Argentina de Astronomia La Plata Argentina*, *6*, 41.

Shapley, H., & Curtis, H. D. (1921, may). The Scale of the Universe. *Bulletin of the National Research Council, Vol. 2, Part 3, No. 11, p. 171-217*, *2*, 171-217.

Simard, L. (1998, Jan). GIM2D: an IRAF package for the Quantitative Morphology Analysis of Distant Galaxies. In R. Albrecht, R. N. Hook, & H. A. Bushouse (Eds.), *Astronomical data analysis software and systems vii* (Vol. 145, p. 108).

Swinbank, A. M., Harrison, C. M., Trayford, J., Schaller, M., Smail, I., Schaye, J., ... Stott, J. P. (2017, May). Angular momentum evolution of galaxies over the past 10 Gyr: a MUSE and KMOS dynamical survey of 400 star-forming galaxies from z = 0.3 to 1.7. *Monthly Notices of the Royal Astronomical Society*, *467*(3), 3140-3159. doi: 10.1093/mnras/stx201

Trimble, V. (1995, Dec). The 1920 Shapley-Curtis Discussion: Background, Issues, and Aftermath. *Publications of the Astronomical Society of the Pacific*, *107*, 1133. doi: 10.1086/133671

Zwicky, F. (1933). Die Rotverschiebung von extragalaktischen Nebeln. *Helvetica Physica Acta*, *6*, 110-127.

Zwicky, F. (1937, October). On the Masses of Nebulae and of Clusters of Nebulae. *Astrophysical Journal*, *86*, 217. doi: 10.1086/143864

A Details about morphological classification

We provide in this section a summary of the morphological parameters used by Cassata, Tasca and Zurich for their morphological classification which we used and compared in the present work.

A.1 Non-parametric values

Usual galaxy classification methods rely on the same parameters. Some may use all of them when others only concentrate on a few. We give here a description of the main parameters used for this kind of classification.

A.1.1 Concentration

The first parameter is the concentration. Two quite different definitions exist, the former using flux levels and the latter isophotes. The oldest definition of the concentration comes from Kent (1985). In his paper, he describes it as the log of the ratio between the radii enclosing 80% and 20% of the "total" luminosity (respectively r_{80} and r_{20})

$$C = 5 \log \frac{r_{80}}{r_{20}} \tag{20}$$

The concentration parameter can vary in theory from 1 to infinity. The parameter C as defined in Eq. 20 should be interpreted cautiously as many definitions of the "total" luminosity (sometimes also called total flux) are used. Some authors who have performed a morphological modelling might call total luminosity the integrated flux up to infinity of their best fit model. Others might use the flux within some fixed aperture (generally a multiplicative factor of the Petrosian radius r_{p}), such as $2\,r_{\mathrm{p}}$ in Bershady et al. (2000), or $1.5\,r_{\mathrm{p}}$ in Lotz et al. (2004).

Another definition comes from Abraham et al. (1994). In this case, second order moments of the image are computed in order to find an outer elliptical aperture with an area similar to that of the galaxy up to some isophotal limit (generally 2σ). From this ellipse, the semi-major axis can be obtained. A second semi-major axis 30% smaller is derived and an inner ellipse with the same shape is defined. The concentration parameter is then computed as the ratio between the flux within the outer and the inner apertures

$$C = \frac{\sum_{(x,y)\in\mathcal{E}_{\mathrm{in}}} I(x,y)}{\sum_{(x,y)\in\mathcal{E}_{\mathrm{out}}} I(x,y)} \tag{21}$$

where $\mathcal{E}_{\mathrm{in}}$ and $\mathcal{E}_{\mathrm{out}}$ are respectively the inner and outer ellipses. This definition therefore yields a concentration parameter C between 0 and 1.

32

A.1.2   Asymmetry

The asymmetry parameter defines how symmetric/asymmetric a galaxy is. A related parameter was first introduced by Schade et al. (1995) in order to classify galaxies as being symmetric or not, though its definition differed by using a combination of original and residual maps in its computation.

The most common definition of the asymmetry A comes from Abraham et al. (1996). The map is rotated by 180° and is subtracted to the original map. The asymmetry parameter is then computed as half the ratio between the total integrated intensity amplitude in the self-subtracted map and the total intensity amplitude in the original map. Using an absolute value will add a positive term in A from background signal. To get rid of it, the same calculation is performed for an aperture of the same size with only background signal and this value is subtracted from the previous one, i.e.

$$A = \frac{\sum_{i,j} |I(i,j) - I_{180}(i,j)|}{2 \sum_{i,j} |I(i,j)|} - B_{180} \tag{22}$$

where I_{180} designates the rotated map and B_{180} is the average asymmetry of the background. This definition, though commonly used, is sometimes replaced by a similar one where square brackets are used instead of absolute values. This is for instance the case in Conselice (1997). Nevertheless, both definitions yield values of A between 0 (completely symmetrical) and 1 (completely asymmetrical).

The value of A can be quite sensitive to the choice of the centre. Methods for finding the best centre position include using the brightest point in a smoothed map or iterating over X and Y till A is minimised.

A.1.3   Gini coefficient